

# Shadows of spherically symmetric black holes and naked singularities

Rajibul Shaikh<sup>1,\*</sup>, Prashant Kocherlakota<sup>1,†</sup>, Ramesh Narayan<sup>2,‡</sup> and Pankaj S. Joshi<sup>1,§</sup>

<sup>1</sup> *Tata Institute of Fundamental Research,  
Homi Bhabha Road, Colaba, Mumbai 400005, India and*

<sup>2</sup> *Harvard-Smithsonian Center for Astrophysics,  
60 Garden Street, Cambridge, MA 02138, USA*

## Abstract

We compare shadows cast by Schwarzschild black holes with those produced by two classes of naked singularities that result from gravitational collapse of spherically symmetric matter. The latter models consist of an interior naked singularity spacetime restricted to radii  $r \leq R_b$ , matched to Schwarzschild spacetime outside the boundary radius  $R_b$ . While a black hole always has a photon sphere and always casts a shadow, we find that the naked singularity models have photon spheres only if a certain parameter  $M_0$  that characterizes these models satisfies  $M_0 \geq 2/3$ , or equivalently, if  $R_b \leq 3M$ , where  $M$  is the total mass of the object. Such models do produce shadows. However, models with  $M_0 < 2/3$  (or  $R_b > 3M$ ) have no photon sphere and do not produce a shadow. Instead, they produce an interesting “full-moon” image. These results imply that the presence of a shadow does not by itself prove that a compact object is necessarily a black hole. The object could be a naked singularity with  $M_0 \geq 2/3$ , and we will need other observational clues to distinguish the two possibilities. On the other hand, the presence of a full-moon image would certainly rule out a black hole and might suggest a naked singularity with  $M_0 < 2/3$ . It would be worthwhile to generalize the present study, which is restricted to spherically symmetric models, to rotating black holes and naked singularities.

---

\* [rajibul.shaikh@tifr.res.in](mailto:rajibul.shaikh@tifr.res.in)

† [k.prashant@tifr.res.in](mailto:k.prashant@tifr.res.in)

‡ [rnarayan@cfa.harvard.edu](mailto:rnarayan@cfa.harvard.edu)

§ [psj@tifr.res.in](mailto:psj@tifr.res.in)

## I. INTRODUCTION

Currently, there is compelling evidence for the presence of compact regions in the universe with very large mass, and this is interpreted as strong indirect evidence for the existence of black holes. The compact object Sagittarius A\* (Sgr A\*) at our Galactic Center, with a mass of  $4 \times 10^6 M_\odot$ , is the best example of such an object [1, 2], and there is considerable evidence for similar objects of even greater mass at the centers of many other galaxies [3]. However, direct evidence for the presence of a black hole requires actual detection of the event horizon, the surface that encloses the compact interior of the black hole, and from where no material particles or light rays can escape. A number of tests have been proposed to confirm the presence of event horizons in black hole candidates [4–6]. The evidence is strong but, of necessity [7], not conclusive.

With the purpose of strengthening the evidence for the presence of a black hole in Sgr A\*, as well as in the nucleus of the nearby galaxy M87, the event horizon telescope [8, 9], an Earth-spanning millimeter-wave interferometer, is being constructed and has begun collecting data. While nothing escapes from the interior of a black hole, the exterior spacetime has a photon sphere which is predicted to create a characteristic shadow-like image of the radiation emitted by an accretion flow around the black hole [10–12]. The goal of the EHT is to verify the presence of this shadow at mm wavelengths in the image of Sgr A\*. This would add considerably to the evidence that Sgr A\* is a black hole.

Typically, compact black hole-like objects in the universe are created by gravitational collapse of matter, e.g., from the collapse of massive stars at the end of their life-cycles. Having exhausted their internal nuclear fuel, these stars end up as compact stellar-mass objects. Alternatively, clustering of matter in the central region of a galaxy may generate a massive compact object, which may then grow further in mass by accretion.

It is worth noting here that one of the major and frontier unresolved problem in gravitation physics, at the very foundation of black hole physics and its astrophysical applications, is showing that all physically reasonable gravitational collapses end up producing a black hole only. In that case, the spacetime singularity resulting from collapse, which is a necessary implication of general relativity, will be always hidden within an event horizon, which allows no signals to be seen from the vicinity of the spacetime singularity. The hypothesis that this is necessarily so is called the cosmic censorship conjecture [13]. When the singularity of collapse is not covered by an event horizon, it is called a naked singularity, which is in principle visible to faraway observers in the universe. The exciting prospect in this later case is the possibility to have observable signatures from ultra-strong gravity regions near

the singularity. Despite the past five decades of serious efforts, the censorship remains an unproven conjecture, to the extent that we do not even have any definite mathematical formulation for the same.

On the other hand, many studies of gravitational collapse have been carried out and it turns out that the end state of collapse is not necessarily a black hole always. This important key issue was studied in considerable detail in past decades and the formation of event horizons, trapped surfaces and apparent horizons has been investigated in different scenarios [14, 15]. While the general theory of relativity necessarily predicts the occurrence of a spacetime singularity as a result of collapse for a wide range of initial conditions, it turns out that the formation or otherwise of the event horizon, as well as the actual epoch of horizon formation, are governed by the specific regular initial conditions from which the collapse evolves. Therefore, the final state of continual collapse turns out to be either a black hole or a naked singularity, depending on the initial conditions and the allowed evolutions by the Einstein equations, in many physically reasonable collapse scenarios.

Recently, we investigated physically reasonable gravitational collapse scenarios that end up as naked singularities [16, 17], and computed various properties of these spacetimes, such as the nature of stable circular orbits and the spectra of accretion disks. We found that spectra, in particular, may be helpful to discriminate between black holes and naked singularities.

The purpose of the present work is to examine shadows and images of these naked singularity models and to compare them with the images we expect with black holes. The goal is to check whether the images corresponding to the two kinds of model are clearly distinguishable. The interesting conclusion is that, while black holes always cast a shadow, naked singularities may or may not, depending on the specific structure of the singularity. Therefore, while black holes imply shadows, the converse is not true. A shadow could be produced by certain naked singularities as well.

The plan of the paper is as follows. In §II, we briefly review the collapse models we use here, and outline some of their properties. In §III, we investigate geodesic motion, unstable photon orbits and the resulting shadows. In §IV, we study gravitational lensing and relativistic images in the various spacetimes. In §V, we consider a simple accretion model and compute images, which we use to examine how black holes and naked singularities could be distinguished. We then repeat the analysis in §VI using a more realistic accretion flow model and show that the results are largely unchanged. We conclude in §VII with a summary of the key results.

## II. THE BLACK HOLE AND NAKED SINGULARITY SPACETIMES

We compare images and shadows produced by a Schwarzschild black hole with those produced by two different naked singularity spacetimes. The latter two solutions describe the geometry around compact objects formed from gravitational collapse of two different types of fluids.

The first naked singularity solution, which we call JMN-1, is formed from the collapse of matter with zero radial pressure, and is described by the following metric,

$$ds_1^2 = -(1 - M_0) \left( \frac{r}{R_b} \right)^{M_0/(1-M_0)} dt^2 + \frac{dr^2}{1 - M_0} + r^2 (d\theta^2 + \sin^2 \theta d\phi^2), \quad (1)$$

where the parameter  $M_0$  is limited to the range  $0 \leq M_0 \leq 4/5$  (the upper limit corresponds to the requirement that the sound speed should not exceed unity, see [16]). The matter content of this spacetime has the following energy density  $\rho$ , radial pressure  $p_r$ , and tangential pressure  $p_\theta$ :

$$\rho = \frac{M_0}{r^2}, \quad p_r = 0, \quad p_\theta = \frac{M_0}{4(1 - M_0)} \rho = \frac{M_0^2}{4(1 - M_0)} \frac{1}{r^2}. \quad (2)$$

There is a non-zero tangential pressure, but the radial pressure is assumed to vanish.

The second naked singularity solution, which we call JMN-2, is the end state of collapse of a spherical cloud with non-zero radial pressure, for example, a perfect fluid cloud with an equation of state  $p = k\rho$ . The coefficient  $k$  could vary in general with radius, but has a constant value in the neighborhood of the center. This spacetime is described by the metric [17],

$$ds_2^2 = -\frac{1}{16\lambda^2(2 - \lambda^2)} \left[ (1 + \lambda)^2 \left( \frac{r}{R_b} \right)^{1-\lambda} - (1 - \lambda)^2 \left( \frac{r}{R_b} \right)^{1+\lambda} \right]^2 dt^2 \\ + (2 - \lambda^2) dr^2 + r^2 (d\theta^2 + \sin^2 \theta d\phi^2), \quad (3)$$

where  $0 \leq \lambda < 1$ . The expressions for the energy density and pressure can be found in [17]. For easier comparison with the JMN-1 model, we define a parameter  $M_0$ ,

$$M_0 = \frac{1 - \lambda^2}{2 - \lambda^2}, \quad (4)$$

which represents an alternative way (instead of  $\lambda$ ) of parametrizing JMN-2.

Both JMN-1 and JMN-2 contain a time-like naked singularity at  $r = 0$ . While there is central singularity present, there are no trapped surfaces forming in the spacetime, thus causing the naked singularity. and both are matched at their outer radius  $r = R_b$  to the Schwarzschild geometry,

$$ds_0^2 = - \left( 1 - \frac{2M}{r} \right) dt^2 + \frac{dr^2}{1 - \frac{2M}{r}} + r^2 (d\theta^2 + \sin^2 \theta d\phi^2). \quad (5)$$

In both cases, the total mass  $M$  is given by

$$M = \frac{1}{2}M_0R_b. \quad (6)$$

All three spacetimes under consideration, viz., the two naked singularity spacetimes and the Schwarzschild spacetime, can be written in the general form,

$$ds_i^2 = -f_i(r)dt^2 + \frac{dr^2}{g_i(r)} + r^2(d\theta^2 + \sin^2\theta d\phi^2), \quad (7)$$

where the JMN-1 spacetime corresponds to  $i = 1$ , hence

$$f_1(r) = (1 - M_0) \left( \frac{r}{R_b} \right)^{M_0/(1-M_0)}, \quad g_1(r) = (1 - M_0), \quad (8)$$

the JMN-2 spacetime corresponds to  $i = 2$  and has

$$f_2(r) = \frac{1}{16\lambda^2(2 - \lambda^2)} \left[ (1 + \lambda)^2 \left( \frac{r}{R_b} \right)^{1-\lambda} - (1 - \lambda)^2 \left( \frac{r}{R_b} \right)^{1+\lambda} \right]^2, \quad g_2(r) = \frac{1}{2 - \lambda^2}, \quad (9)$$

and the Schwarzschild spacetime corresponds to  $i = 0$  and has

$$f_0(r) = g_0(r) = \left( 1 - \frac{2M}{r} \right). \quad (10)$$

### III. SHADOWS OF JMN NAKED SINGULARITIES AND SCHWARZSCHILD BLACK HOLE

The shadow structures for the different spacetimes are determined by the properties of null geodesics in these spacetimes. We therefore begin with a discussion of this topic. We consider an extended source of radiation on the far side of the compact object. Photons from the source traverse the spacetime of the black hole or naked singularity, get deflected, and reach the observer. As viewed by the observer, we are interested in those directions for which no (or very little) radiation is received. The union of these directions constitutes the shadow of the gravitating object.

#### A. Geodesic motion and unstable photon orbits

The Lagrangian describing the motion of a photon in the spacetime geometry (7) is given by

$$2\mathcal{L} = -f_i(r)\dot{t}^2 + \frac{\dot{r}^2}{g_i(r)} + r^2\dot{\theta}^2 + r^2\sin^2\theta\dot{\phi}^2, \quad (11)$$

where a dot represents a derivative with respect to the affine parameter. Since the Lagrangian is independent of  $t$  and  $\phi$ , we have two constants of motion:

$$p_t = \frac{\partial \mathcal{L}}{\partial \dot{t}} = -f_i(r)\dot{t} = -E, \quad (12)$$

$$p_\phi = \frac{\partial \mathcal{L}}{\partial \dot{\phi}} = r^2 \sin^2 \theta \dot{\phi} = L, \quad (13)$$

where  $E$  and  $L$  are, respectively, the energy and angular momentum of the photon. Using the null geodesics condition  $g_{\mu\nu}\dot{x}^\mu\dot{x}^\nu = 0$ , we obtain

$$\frac{1}{g_i}\dot{r}^2 + r^2\dot{\theta}^2 = \frac{r^2 \sin^2 \theta E^2 - f_i L^2}{f_i r^2 \sin^2 \theta}. \quad (14)$$

Since our spacetimes are spherically symmetric, the shadows and images will be circularly symmetric in the observer sky. Thus the intensity will be a function only of the impact parameter  $b = L/E$  with respect to the center of the spacetime, and will be independent of the azimuthal angle  $\theta$ . Therefore, we can simply choose  $\theta = \pi/2$ ,  $\dot{\theta} = 0$ , and obtain all our results for this case. The same results can then be applied to all  $\theta$ . Setting  $\theta = \pi/2$  and  $\dot{\theta} = 0$ , we obtain

$$\frac{f_i}{g_i}\dot{r}^2 + V_{eff} = 0, \quad V_{eff} = L^2 \frac{f_i(r)}{r^2} - E^2. \quad (15)$$

The impact parameter  $b$  can be related to the turning point  $r_{tp}$  of a photon, where  $\dot{r} = 0$  and  $V_{eff}(r_{tp}) = 0$ :

$$b = \frac{r_{tp}}{\sqrt{f_i(r_{tp})}}. \quad (16)$$

This expression will be useful in our subsequent studies. Circular photon orbits satisfy  $V_{eff} = 0$  and  $dV_{eff}/dr = 0$ , and we have,

$$x f_{i,x} - 2f_i = 0, \quad (17)$$

$$\frac{b^2}{R_b^2} = \frac{x^2}{f_i}, \quad (18)$$

where  $x = r/R_b$ , and  $f_{i,x}$  represents differentiation of  $f_i$  with respect to  $x$ . Note that the matching surface between the interior naked singularity spacetime and the exterior Schwarzschild spacetime is now at  $x = x_b = 1$ . The photon sphere comprises of circular unstable photon orbits, i.e., orbits that satisfy additionally  $d^2V_{eff}/dr^2 < 0$ .

Equation (17) does not have any non-trivial solution for the two interior JMN spacetimes we are considering. Therefore, there is no photon sphere for either interior JMN spacetime. However, the

JMN spacetimes are matched on the exterior to the Schwarzschild geometry, and the latter spacetime does have unstable photon orbits, that is, a photon sphere at

$$r_{ph} = 3M, \quad x_{ph} \equiv \frac{r_{ph}}{R_b} = \frac{3}{2}M_0. \quad (19)$$

Therefore, the existence or not of a photon sphere in the naked singularity models depends on the relative sizes of  $x_{ph}$  and the matching radius  $x_b$ . A photon sphere exists whenever the following conditions, which are all equivalent, are satisfied

$$R_b \leq 3M, \quad x_{ph} \geq x_b, \quad M_0 \geq \frac{2}{3}. \quad (20)$$

There is no photon sphere when  $M_0 < 2/3$ , or equivalently, when  $R_b > 3M$ .

The JMN-1 spacetime satisfies reasonable physical conditions (e.g., sound speed less than unity) for the parameter range  $0 < M_0 < 4/5$ . The subset of these models with  $2/3 \leq M_0 < 4/5$  have photon spheres, while the rest do not. The JMN-2 spacetime is parametrised by  $0 \leq \lambda = \sqrt{(1 - 2M_0)/(1 - M_0)} \leq 1$ , which means that the allowed range of  $M_0$  is  $0 \leq M_0 \leq 1/2$ . Thus, JMN-2 is devoid of a photon sphere for the entire allowed range of parameter values. It should be noted that for the cases for which photon spheres exist, they are always located in the exterior Schwarzschild geometry. Setting  $x = x_{ph} = 3M_0/2$  in Eq. (18), we obtain

$$b_{ph}^2 = \frac{27}{4}M_0^2 R_b^2 = 27M^2, \quad (21)$$

which is the same equation as that obtained for the Schwarzschild black hole. The only difference in the case of the JMN spacetimes is that we have the additional requirement,  $M_0 \geq 2/3$  (or  $R_b \leq 3M$ ), in order to have a photon sphere. In the above discussion,  $b_{ph}$  is the critical impact parameter of a photon on an unstable photon orbit.

## B. Shadows

The unstable photon orbits constitute the photon sphere, and they define the boundary of the shadow cast by a compact object. Photons from a distant source with impact parameter  $b$  larger than the critical impact parameter  $b_{ph}$ , i.e.,

$$b^2 > 27M^2, \quad (22)$$

remain outside the photon sphere and reach the observer. However, photons with impact parameters smaller than the critical impact parameter are captured within the photon sphere and do not reach the

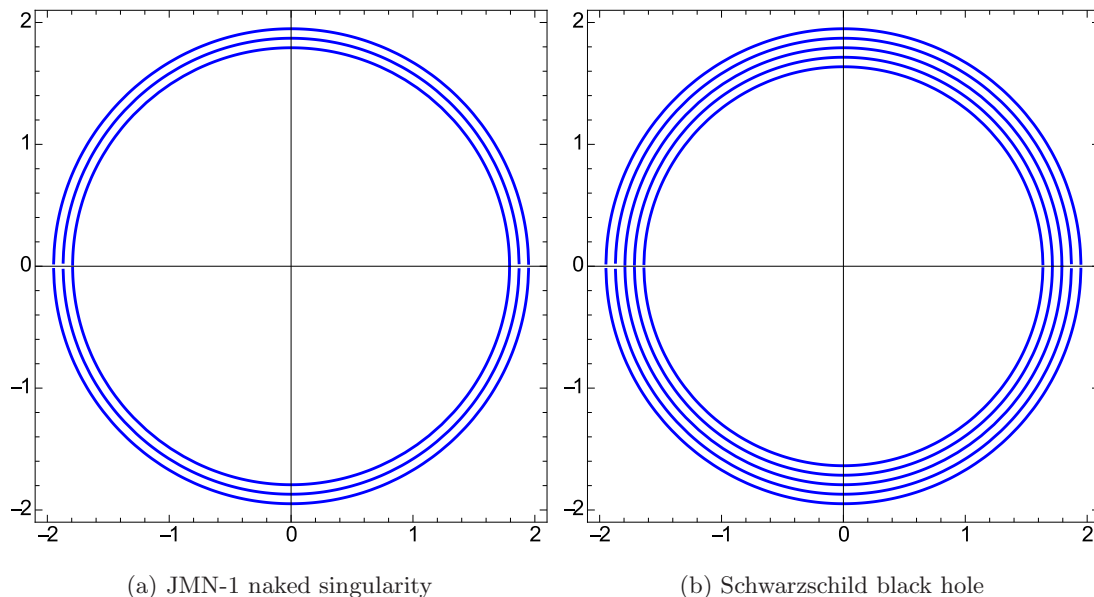


FIG. 1. Shadows cast by (a) the JMN-1 naked singularity, matched to the exterior Schwarzschild spacetime at  $x = x_b = 1$ , for  $M_0 = 0.75, 0.72, 0.69, 0.66, 0.63$  (from outer to inner), in the units of  $R_b$ , and (b) the Schwarzschild black hole for same different masses (from outer to inner). For  $M_0 < 2/3$ , the JMN-1 naked singularity does not cast any shadow. Here different  $M_0$  values mean different total masses.

observer, thereby creating dark spots in the observer's sky. The union of these dark spots constitutes the shadow. Therefore, the apparent shape of the shadow projected in the observer's sky is a circular disk whose radius is given by the critical impact parameter  $b_{ph} = 3\sqrt{3}M$ .

Figure 1 shows the shapes of shadows cast by the JMN-1 naked singularity and the Schwarzschild black hole. The circles represent the outer boundaries of the shadows. In the case of the black hole, shadows exist for all  $M$ . However, in the case of the JMN-1 naked singularity, depending on the value of  $M_0$ , a shadow may either form ( $M_0 \geq 2/3$ ), or not form ( $M_0 < 2/3$ ). As we noted earlier, in the case of the JMN-2 naked singularity there is no photon sphere, and therefore this spacetime does not cast any shadow.

#### IV. GRAVITATIONAL LENSING AND RELATIVISTIC IMAGES

Since the shadows and images are the result of strong gravitational lensing, we now study lensing by the JMN naked singularities. From §III, we obtain

$$\frac{d\phi}{dr} = \frac{1}{r^2 \sqrt{g_i(r)}} \frac{1}{\sqrt{\frac{1}{b^2 f_i(r)} - \frac{1}{r^2}}}, \quad (23)$$



where  $b$  is the impact parameter. Defining  $u = R_b/r$ , we obtain the deflection angle

$$\alpha = 2 \int_0^{u_{tp}} \frac{1}{\sqrt{g_i}} \frac{1}{\sqrt{\frac{1}{b^2 f_i(u)} - u^2}} du - \pi, \quad (24)$$

where

$$\bar{b} = \frac{b}{R_b}, \quad u_{tp} = \frac{R_b}{r_{tp}}, \quad (25)$$

and  $r_{tp}$  is the turning point given by  $dr/d\phi = 0$ . For the spacetimes under consideration, the dimensionless impact parameter  $\bar{b}$  is given by (see Eq. 16)

$$\bar{b} = \frac{1}{u_{tp} \sqrt{f_i(u_{tp})}}. \quad (26)$$

Note that when  $r_{tp} = R_b$ ,  $u_{tp} = 1$ . Therefore, if  $u_{tp} < 1$ , then the photon does not enter the interior of the JMN metric. In that case, the deflection is given by Eqs. (24) and (26) with  $f_i(r)$  and  $g_i(r)$  given by the exterior Schwarzschild metric. However, if the photon does enter the JMN metric and has its turning point in the interior ( $r_{tp} < R_b$ , i.e.,  $u_{tp} > 1$ ), then the deflection angle can be written as [18]

$$\alpha = 2 \int_0^1 \frac{1}{\sqrt{g_0}} \frac{1}{\sqrt{\frac{1}{b^2 f_0(u)} - u^2}} du + 2 \int_1^{u_{tp}} \frac{1}{\sqrt{g_{1,2}}} \frac{1}{\sqrt{\frac{1}{b^2 f_{1,2}(u)} - u^2}} du - \pi, \quad (27)$$

where  $f_{1,2}$  refer to the JMN-1 or JMN-2 models, respectively, and the impact parameter  $\bar{b}$  is given by Eq. (26). The first term in Eq. (27) is the contribution from the exterior Schwarzschild geometry and the second term is that from the interior JMN metric,  $\alpha_{\text{JMN1}}$  or  $\alpha_{\text{JMN2}}$ .

Because of its simple form, here we focus on the JMN-1 naked singularity. As discussed in §III, a photon sphere exists for  $M_0 \geq 2/3$  and the photon sphere lies in the exterior Schwarzschild geometry. As a result, all the photons which participate in the image formation have their turning points outside of the photon sphere. Therefore, in this case, there is no difference in lensing behavior between the JMN-1 naked singularity and the Schwarzschild black hole. On the other hand, since there is no photon sphere for  $M_0 < 2/3$ , photons may enter the interior of the JMN-1 spacetime and experience a turning point because of the infinite potential barrier at the singularity. Therefore, for this range of  $M_0$ , there is a clear distinction between the lensing behavior of the JMN-1 naked singularity and that of the Schwarzschild black hole.

For  $M_0 < 2/3$ , the contribution of the JMN-1 spacetime to the deflection angle,  $\alpha_{\text{JMN1}}$ , can be

obtained analytically by a change of variables to  $z = u^{(2-3M_0)/2(1-M_0)}$ . We then obtain

$$\begin{aligned}\alpha_{\text{JMN1}} &= 2 \int_1^{u_{tp}} \frac{du}{\sqrt{g_1}} \frac{1}{\sqrt{\frac{1}{b^2 f_1(u)} - u^2}} \\ &= \frac{4\sqrt{1-M_0}}{2-3M_0} \int_1^{z_{tp}} \frac{dz}{\sqrt{\frac{1}{b^2(1-M_0)} - z^2}} \\ &= \frac{2\sqrt{1-M_0}}{2-3M_0} \left[ \pi - 2 \sin^{-1} \left( \frac{r_{tp}}{R_b} \right)^{\frac{2-3M_0}{2(1-M_0)}} \right],\end{aligned}\quad (28)$$

where  $r_{tp} \leq R_b$ .

The analytical expression of the contribution due to the Schwarzschild geometry in the exterior of the JMN-1 model is the same as that of a Schwarzschild black hole and can be found in [19]. Figure (2) shows a plot of the deflection angle as a function of  $u_{tp}$ . Since a photon sphere exists for  $M_0 \geq 2/3$ , the deflection angle diverges as the turning point approaches the photon sphere. This divergence is logarithmic [20]. Therefore, theoretically, there will be an infinite number of images just outside the photon sphere.

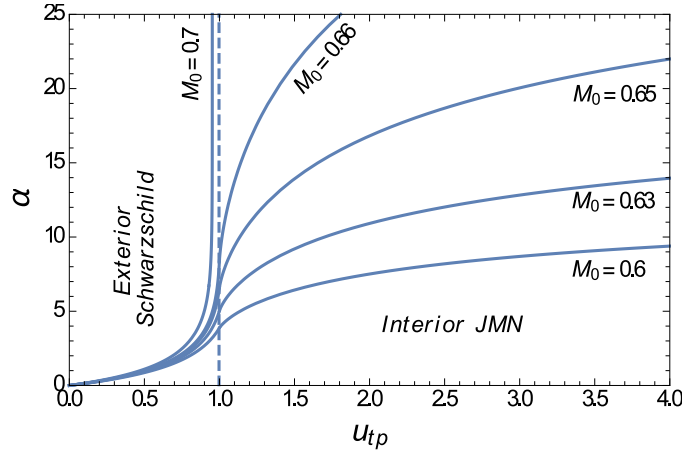


FIG. 2. Deflection angle  $\alpha$  as a function of  $u_{tp}$  of light rays for the JMN-1 naked singularity matched with an exterior Schwarzschild geometry. The vertical dashed line shows the boundary between the two geometries.

For the JMN-1 naked singularity model with  $M_0 < 2/3$ , although there is no photon sphere, the deflection angle can still be large because, depending on the impact parameter, light rays may wind around the singularity several times. Due to this large bending, there can be many relativistic rings even for  $M_0 < 2/3$ .

In the following, for simplicity, we assume that the observer, the lens, and the distant point light source are all aligned. We also consider that the observer and the light source are far away from

the lens. Therefore, in the observer's sky, the relativistic images will be concentric rings (known as relativistic Einstein rings) of radii given by the corresponding impact parameters  $b(r_{tp})$ . These impact parameter values  $b(r_{tp})$  can be obtained by solving  $\alpha \simeq 2\pi n$ , where  $n$  is the ring number [20].

Figure 3 shows the relativistic Einstein rings in the observer's sky. In the case of the JMN-1 naked singularity with  $M_0 \geq 2/3$  and the Schwarzschild black hole, all the relativistic images are clumped together outside the photon sphere, which forms the outer boundary of the shadow. The radius of the innermost image in the observer's sky is given by the minimum critical impact parameter  $b_{ph}$ . Photons with impact parameter less than  $b_{ph}$  are absorbed by the photon sphere. Hence, in this case, there is a shadow and many relativistic images clumped together just outside the edge of the shadow.

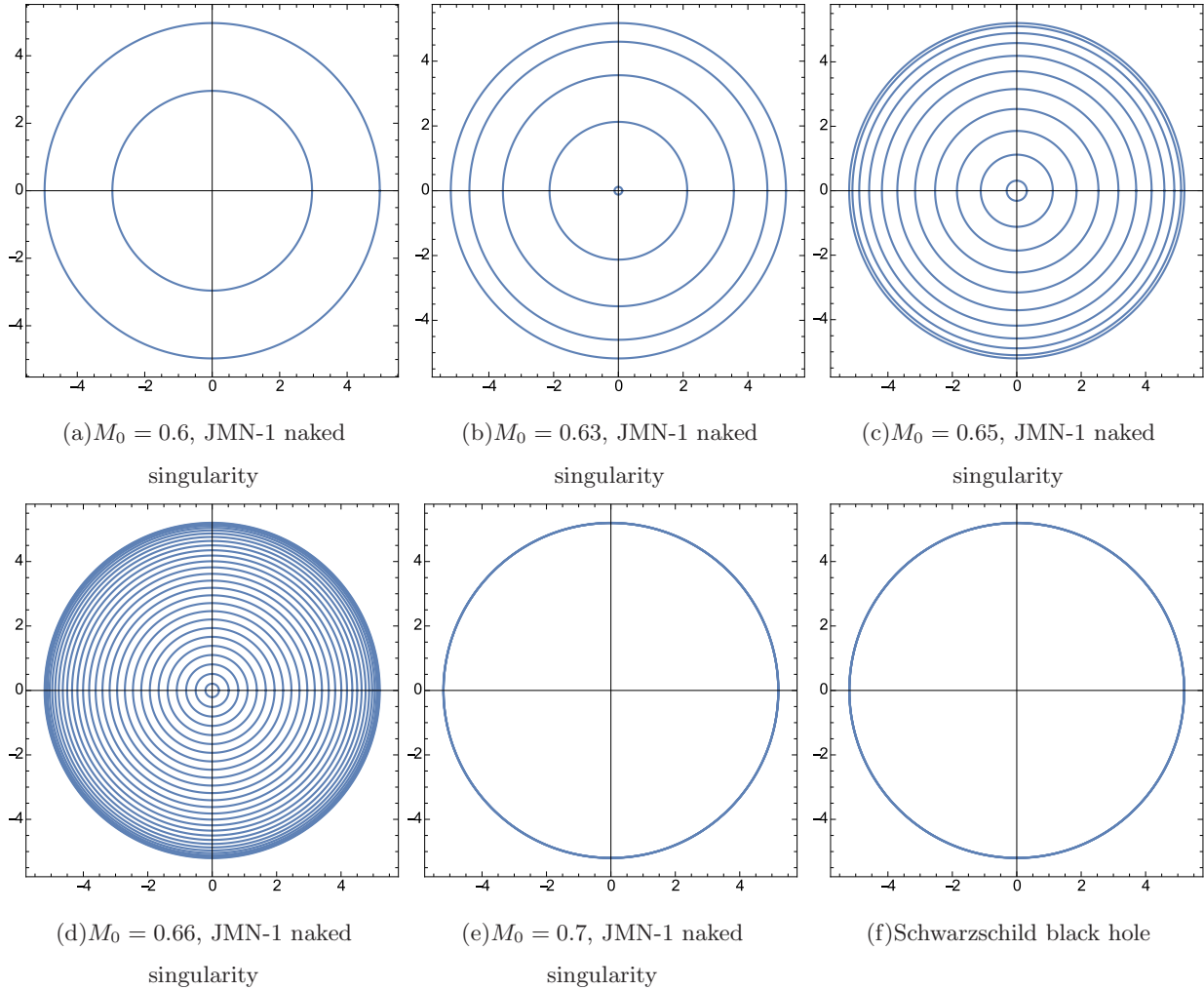


FIG. 3. Relativistic Einstein ring images due to gravitational lensing by (a-e) the JMN-1 naked singularity with different values of  $M_0$ , and (f) the Schwarzschild black hole. The axes are in units of  $M$ .

As an aside we note that, besides the relativistic Einstein rings discussed here, there is a standard

Einstein ring formed as a result of weak deflection of light (weak deflection occurs when  $M/r_{tp} \ll 1$ ). For all physically reasonable  $M_0$  values, weak deflection and the traditional Einstein ring occur in the exterior Schwarzschild geometry. Therefore, the traditional Einstein ring of the JMN-1 naked singularity will be the same as that due to the Schwarzschild black hole (differences may arise when  $M_0$  is uninterestingly small).

In the case of the JMN-1 naked singularity with  $M_0 < 2/3$ , there is no photon sphere and hence there is no capture of photons. As a result, we have many distinct rings corresponding to different relativistic images. The density of relativistic images increases as  $M_0$  approaches  $2/3$ . This is illustrated in Figure 3.

The discussion so far is for a single point source aligned perfectly behind the lens. However, in realistic situations, we may have many light sources in different directions and at different distances around the lens. The angular positions of the relativistic images formed due to each source will be different. Therefore, in the observer's sky, there will be numerous relativistic images, which might fill the gaps between the relativistic images shown in Fig. 3. Hence, we may have a smooth continuous image. A similar situation occurs when the black hole or the JMN naked singularity is surrounded by an optically thin emission region, as we discuss in the next section.

## V. SHADOWS AND IMAGES OF OPTICALLY THIN EMISSION REGIONS SURROUNDING BLACK HOLES AND NAKED SINGULARITIES

The previous two sections dealt with distant sources of radiation, far behind the lensing compact object. Here we consider an optically thin, radiating, accretion flow surrounding our compact object and compute the observed image. The difference is that radiation is now emitted over an extended volume near the compact object, including regions inside the photon sphere.

The observed specific intensity  $I_{\nu_o}$  (usually measured in  $\text{erg s}^{-1} \text{cm}^{-2} \text{str}^{-1} \text{Hz}^{-1}$ ) at the observed photon frequency  $\nu_o$  at the point  $(X, Y)$  in the observer's sky is given by [21, 22],

$$I_{\nu_o}(X, Y) = \int_{\gamma} g^3 j(\nu_e) dl_{\text{prop}}, \quad (29)$$

where  $\nu_e$  is the emitted frequency,  $g = \nu_o/\nu_e$  is the redshift factor,  $j(\nu_e)$  is the emitter's rest-frame emissivity per unit volume,  $dl_{\text{prop}} = -k_{\alpha} u_e^{\alpha} d\lambda$  is the infinitesimal proper length in the rest frame of the emitter,  $k^{\mu}$  is the four-velocity of the photons,  $u_e^{\mu}$  is the four-velocity of the emitter, and  $\lambda$  is the affine parameter along the photon path  $\gamma$ . The subscript  $\gamma$  on the integral means that the integration

is evaluated along an observed photon path  $\gamma$ . The redshift factor  $g = \nu_o/\nu_e$  is given by,

$$g = \frac{k_\alpha u_o^\alpha}{k_\beta u_e^\beta}, \quad (30)$$

where  $u_o^\mu = (1, 0, 0, 0)$  is the four-velocity of the distant observer (who is at infinity).

In the spirit of the simple spherically-symmetric spacetimes we are investigating, we consider a correspondingly simple model for the accreting gas. We assume that the gas is in radial free fall [21], with its four-velocity given by,

$$u_e^t = \frac{1}{f_i(r)}, \quad u_e^r = -\sqrt{\frac{g_i(r)}{f_i(r)}} [1 - f_i(r)], \quad u_e^\theta = u_e^\phi = 0. \quad (31)$$

The four-velocity  $k^\mu$  ( $= \dot{x}^\mu$ ) of the photons was already obtained previously. In the subsequent calculations, we will need the following expression,

$$\frac{k^r}{k^t} = \pm f_i(r) \sqrt{g_i(r) \left[ \frac{1}{f_i(r)} - \frac{b^2}{r^2} \right]}, \quad (32)$$

where the sign  $+$ ( $-$ ) is when the photon moves away from (approaches towards) the massive object. The redshift function  $g$  is thus given by,

$$g = \frac{1}{\frac{1}{f_i(r)} - \frac{k_r}{k_t} \sqrt{\frac{g_i(r)}{f_i(r)} (1 - f_i(r))}}. \quad (33)$$

For the specific emissivity, we assume the following simple model [21] in which the emission is monochromatic with emitter's rest-frame frequency  $\nu_*$ , and the emission has a  $1/r^2$  radial profile:

$$j(\nu_e) \propto \frac{\delta(\nu_e - \nu_*)}{r^2}, \quad (34)$$

where  $\delta$  is the Dirac delta function. Finally, the proper length in the emitter frame is given by

$$dl_{\text{prop}} = -k_\alpha u_e^\alpha d\lambda = -\frac{k_t}{gk^r} dr. \quad (35)$$

Integrating Eq. (29) over all the observed frequencies, we obtain the observed photon intensity [21]

$$I_{\text{obs}}(X, Y) \propto - \int_\gamma \frac{g^3 k_t dr}{r^2 k^r}. \quad (36)$$

Note that the intensity map in the observer's sky will be circularly symmetric, with the impact parameter  $b$  of any equi-intensity circle given by  $X^2 + Y^2 = b^2$ . Figures 4 and 5 show intensity maps of the image of the above model accretion flow for the Schwarzschild black hole and the two JMN naked singularities.

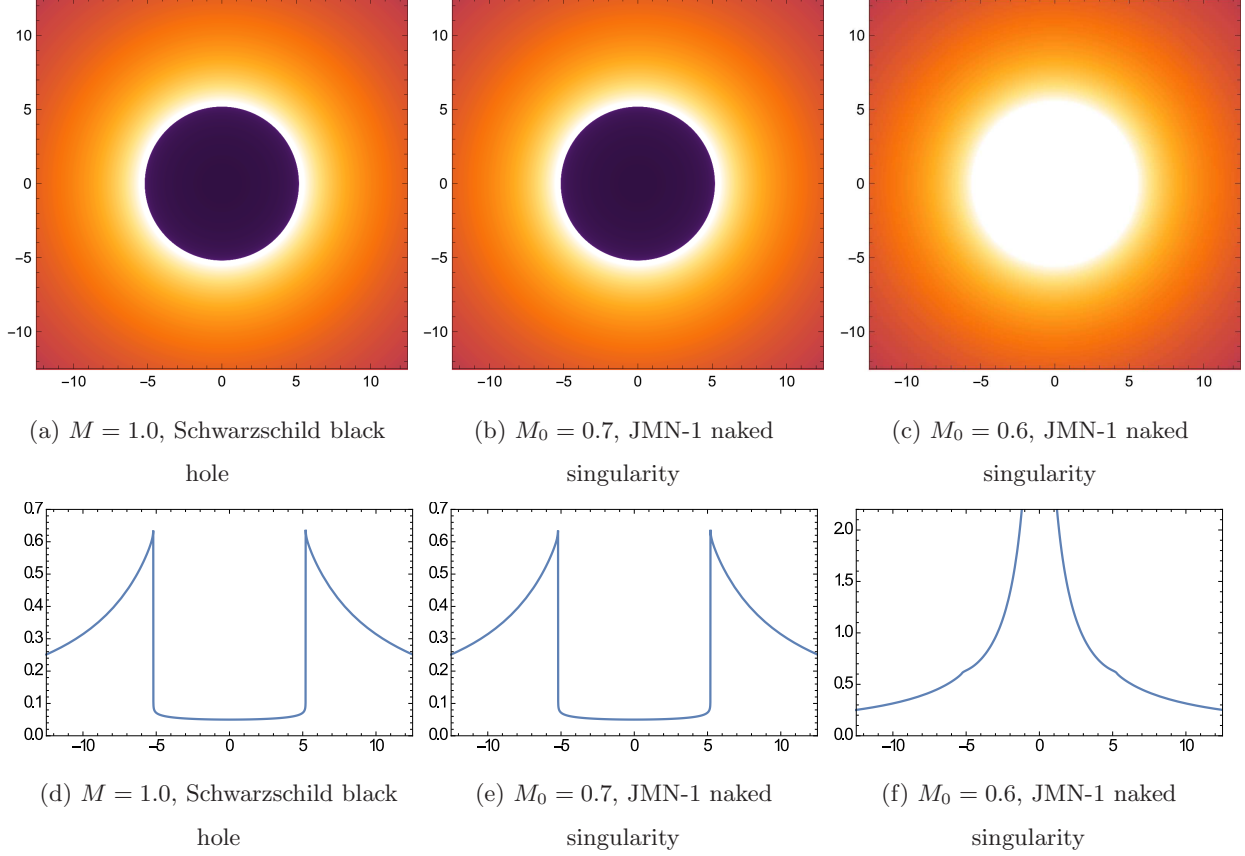


FIG. 4. The upper row shows the image of an optically thin emission region surrounding the Schwarzschild black hole (a) and the JMN-1 naked singularity for  $M_0 = 0.7$  (b) and  $M_0 = 0.6$  (c). The corresponding intensity distributions as a function of the impact parameter are shown in the lower row. All spatial coordinates are in units of  $M$ .

We now note the qualitative differences in the shadows and images produced by the Schwarzschild black hole and the JMN naked singularities. As expected, the Schwarzschild black hole always casts a shadow (Fig. 4a), though we should point out that the intensity inside the shadow does not quite go to zero as in the previous sections but has a small finite value (Fig. 4d). This difference is because the accretion flow emits radiation inside the photon sphere and a small fraction of this radiation is able to escape to infinity.

In the case of the JMN-1 naked singularity, if the model has a photon sphere ( $M_0 \geq 2/3$ ,  $R_b \leq 3M$ ), then its shadow and image (Fig. 4b) mimic those of the Schwarzschild black hole. However, if the JMN-1 naked singularity does not have a photon sphere, then it casts a “full-moon” image (Fig. 4c), which is remarkably different from the images in Figs. 4a and 4b. Notably, the image is quite unlike the image obtained with the Schwarzschild black hole (Fig. 4a). Such a difference, if observationally detected, could greatly help distinguish a naked singularity from a black hole.

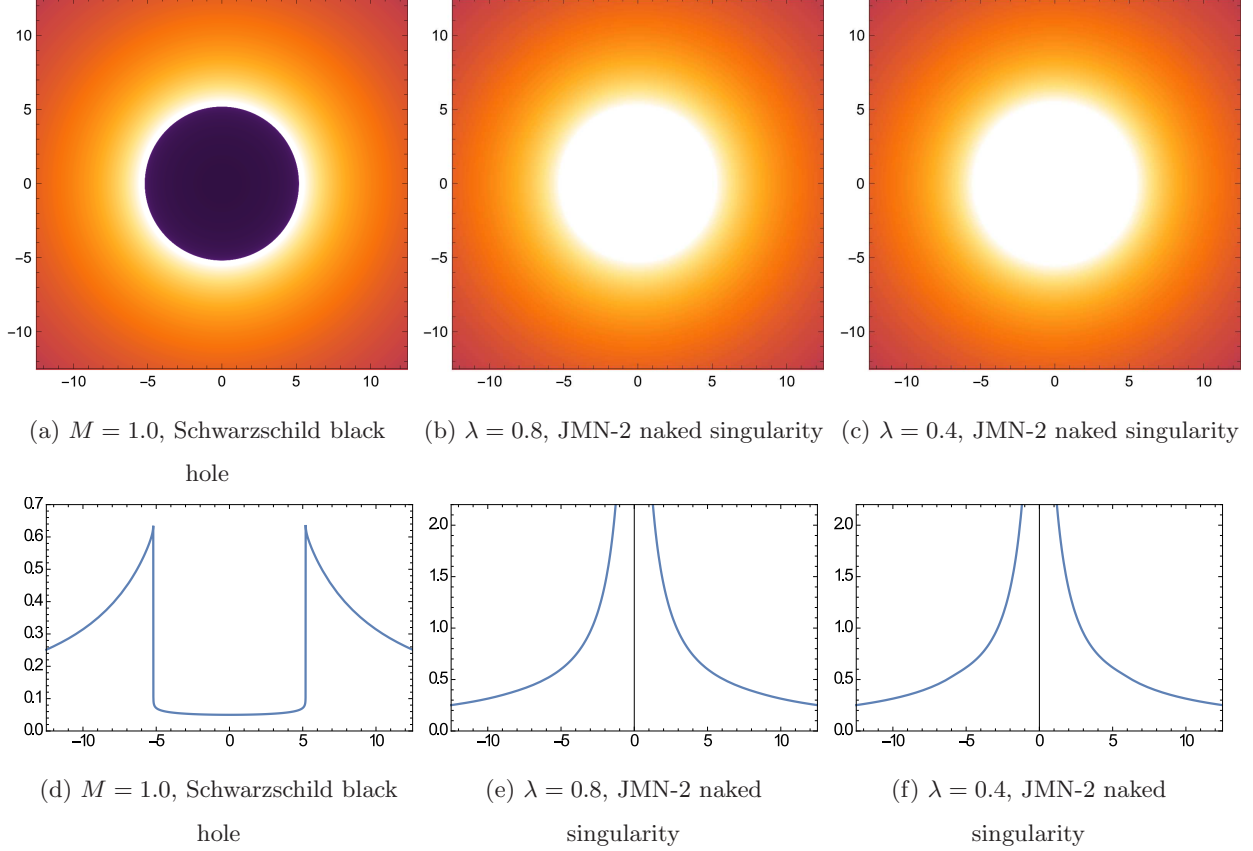


FIG. 5. The upper row shows the image of an optically thin emission region surrounding the Schwarzschild black hole (a) and the JMN-2 naked singularity for  $\lambda = 0.8$  (b) and  $\lambda = 0.4$  (c). The corresponding intensity distributions as a function of the impact parameter are shown in the lower row. All spatial coordinates are in units of  $M$ .

The JMN-2 naked singularity model does not have a photon sphere for any allowed value of the parameter  $\lambda$ . Therefore, the image in this case is always a full-moon, as illustrated in Figs. 5b and 5c.

Our results suggest that, though a naked singularity that has a photon sphere cannot be distinguished from a black hole through observations of the shadow or image, a naked singularity that does not have any photon sphere can be. Note that naked singularities without photon spheres arise when physically realistic collapse models are considered, such as the JMN-2 model [17].

## VI. SHADOWS AND IMAGES OF MORE REALISTIC ACCRETION FLOWS AROUND BLACK HOLES AND NAKED SINGULARITIES

We now describe a more realistic model of the accretion flow with several improvements: (i) we consider a physically motivated emissivity prescription, (ii) we analyze the spectrum of the radiation, and (iii) we avoid the assumption of optically thin emission. As we show, the results are similar to those obtained in §V.

### A. The model

With a view to specializing to the case of the Galactic Center compact object Sagittarius A\* (Sgr A\*), we consider a specific value for the mass of the central object:  $M = 4 \times 10^6 M_\odot$ . As in §V, we assume a spherically symmetric accretion flow, except that we set up the dynamics as in the Bondi accretion model [23]. Thus, we assume that the compact object is embedded in a uniform external medium with a temperature  $T_\infty$  and density  $\rho_\infty$ . We choose  $T_\infty = 10^7$  K, as appropriate for Sgr A\*. For this choice, the Bondi radius, viz., the transition radius where the flow changes in character from a uniform external medium to a freely-falling inner accretion flow, is  $r_B \approx 10^6 M$ . We keep  $\rho_\infty$  as a free parameter which we adjust (thereby tuning the mass accretion rate) such that the luminosity of the resulting accretion flow in the sub-millimeter band matches the observed flux of Sgr A\*. Finally, in the spirit of the Bondi model, and in keeping with §V, we take the velocity profile of the accreting gas to be given by Eq. (31), using the appropriate  $f_i(r)$  and  $g_i(r)$  for each model. However, we modify the radial velocity profile at large radii so that the velocity transitions from the standard free-fall scaling,  $v_r \propto r^{-1/2}$ , at radii inside the Bondi radius to  $v_r \propto r^{-2}$  outside the Bondi radius (for consistency with a uniform gas density at large radii).

We assume that the accreting gas radiates thermal synchrotron and bremsstrahlung, and that the emitted radiation is Compton-scattered as it propagates out of the system. The radiation is treated via a complete radiative transfer model using the transfer code HEROIC [24, 25], with the relativistic enhancements described in [26]. In this code, a large number of ray directions is considered at each point in the accretion flow and the relativistic radiative transfer equation, which considers both emission and absorption, is solved for each ray over a grid of frequencies extending from  $\nu = 10^8$  Hz to  $10^{24}$  Hz. HEROIC was originally written for the Kerr spacetime, and all previous applications were restricted to that spacetime. For the present application, the code was generalized to handle the JMN-1 and JMN-2 spacetimes as well.



The radiative transfer computations enable us to compute the luminosity and radiative spectrum of the emerging radiation for each model. In addition, they also provide the net cooling (if emission dominates) or heating (if absorption dominates) of the accreting gas. We include this cooling/heating information in the energy equation of the accreting gas to solve for the temperature profile  $T(r)$  of the flow (we assume that the gas is a single-temperature plasma). In other words, the only temperature information we input to the model is the boundary condition at infinity ( $T_\infty = 10^7$  K), which sets the location of the Bondi radius. The temperature everywhere else is obtained self-consistently as part of the solution.

The numerical computations are done on a uniform grid in  $\log r$ , with 20 points per decade. The grid extends from an outer radius  $r_{\max} = 10^{6.5}M$  (a factor of a few larger than the Bondi radius) down to an inner radius  $r_{\min}$ . In the case of the Schwarzschild black hole, we choose  $r_{\min}$  to be just outside the horizon, specifically,  $\log r_{\min} = 0.35$ . We assume absorbing boundary conditions at the inner edge of the grid, i.e., any radiation that crosses the horizon is lost from the system. For the two naked singularity models, we would ideally like to set  $r_{\min} = 0$ , but this is not possible with the numerical code. Hence, we use a small non-zero value,  $r_{\min} = 10^{-4}M$ , again assuming absorbing boundary conditions.

## B. Spectra and Temperature Profiles

Figure 6 shows spectra corresponding to five different models: Schwarzschild black hole (red curve), JMN-1 naked singularity with  $M_0 = 0.7$  (green) and  $M_0 = 0.6$  (blue), and JMN-2 naked singularity with  $\lambda = 0.8$  (magenta) and  $\lambda = 0.4$  (cyan). In each model, the mass accretion rate has been adjusted (by varying the density  $\rho_\infty$  of the external medium) so as to give the same luminosity,  $\nu L_\nu = 10^{34.6}$  erg s $^{-1}$  at  $\nu = 200$  GHz (indicated by the black dot), as seen by an observer at infinity. This is approximately the luminosity of Sgr A\*.

As explained in previous sections, of the five spacetime models under consideration, only two have photon spheres, viz., the Schwarzschild black hole and the JMN-1 spacetime with  $M_0 = 0.7$ . Not surprisingly, these two models have nearly identical spectra. The primary peak at  $10^{11}$  Hz in these models is due to thermal synchrotron radiation from hot electrons at radii near the photon sphere. The other peaks are the result of Compton scattering, with a small contribution from bremsstrahlung in the last peak.

The Schwarzschild model and the JMN-1 model with  $M_0 = 0.7$  are much less luminous than the

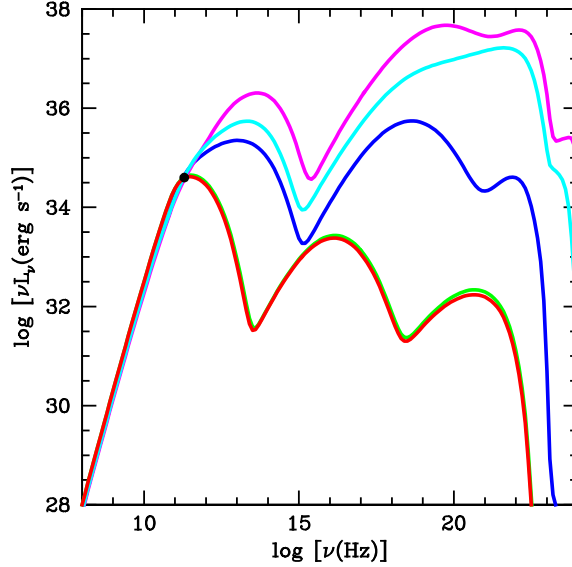


FIG. 6. Spectra of models with a Schwarzschild black hole (red), JMN-1 naked singularity with  $M_0 = 0.7$  (green, under red) and  $M_0 = 0.6$  (blue), and JMN-2 naked singularity with  $\lambda = 0.8$  (magenta) and  $\lambda = 0.4$  (cyan).

other three models (JMN-1  $M_0 = 0.6$ , JMN-2  $\lambda = 0.8$ , JMN-2  $\lambda = 0.4$ ). The latter three spacetimes lack photon spheres and therefore allow radiation to escape more easily from the interior. As a result, they appear to be substantially more luminous, by orders of magnitude, for an observer at infinity

Figure 7 shows the temperature as a function of radius for the same five models. All have essentially the same profile at radii larger than a few  $M$ , where the primary physical effect is compressive heating ( $\rho \propto r^{-3/2}$  implies  $T \propto r^{-1}$  at nonrelativistic temperatures) as gas flows in from the Bondi radius towards the center. At smaller radii ( $r < M$ ), the gas in the four naked singularity models cools to much lower temperatures. Here the gas density is large enough that radiative cooling becomes important. Although much of the radiation is beamed towards small radii, nevertheless enough escapes to cause an enhanced luminosity at infinity. The only exception is the JMN-1  $M_0 = 0.7$  model where, because of the presence of a photon sphere, the amount of radiation that escapes to infinity is highly suppressed.

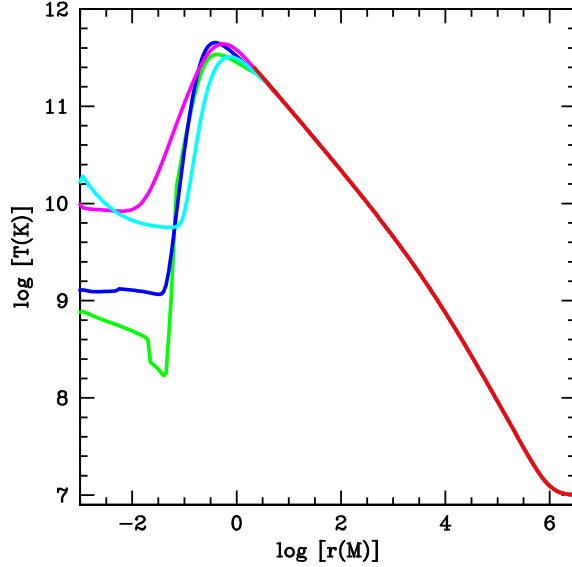


FIG. 7. Radial temperature profiles of models with a Schwarzschild black hole (red), JMN-1 naked singularity with  $M_0 = 0.7$  (green) and  $M_0 = 0.6$  (blue), and JMN-2 naked singularity with  $\lambda = 0.8$  (magenta) and  $\lambda = 0.4$  (cyan).

### C. Images and Shadows

Figure 8 shows images corresponding to the accretion models under discussion. Only radiation with frequencies between 200 and 250 GHz is considered (initial EHT results will be at 230 GHz). The results are qualitatively similar to those shown in Figs. 4 and 5. Specifically, the Schwarzschild black hole and the JMN-1 naked singularity with  $M_0 = 0.7$  have well-defined dark shadows, consistent with the existence of photon spheres in these two models. The other three models, JMN-1 with  $M_0 = 0.6$ , JMN-2 with  $\lambda = 0.8$  and JMN-2 with  $\lambda = 0.4$ , all have filled centers, i.e., they have “full-moon” images, consistent with the lack of photon spheres.

We emphasize that the accretion model considered here, which includes substantially more radiation physics, is significantly different from that in §V. Also, the images in Fig. 8 correspond to the mm-band, whereas in §V we considered monochromatic emission and counted all the radiation. As a result, there are some quantitative differences between Fig. 8 and Figs. 4, 5. The rings around the shadows are somewhat narrower in the present models, and the full-moon images are somewhat smaller in angular size.

One feature that needs discussion is the central dark spot at the center of the full-moon images

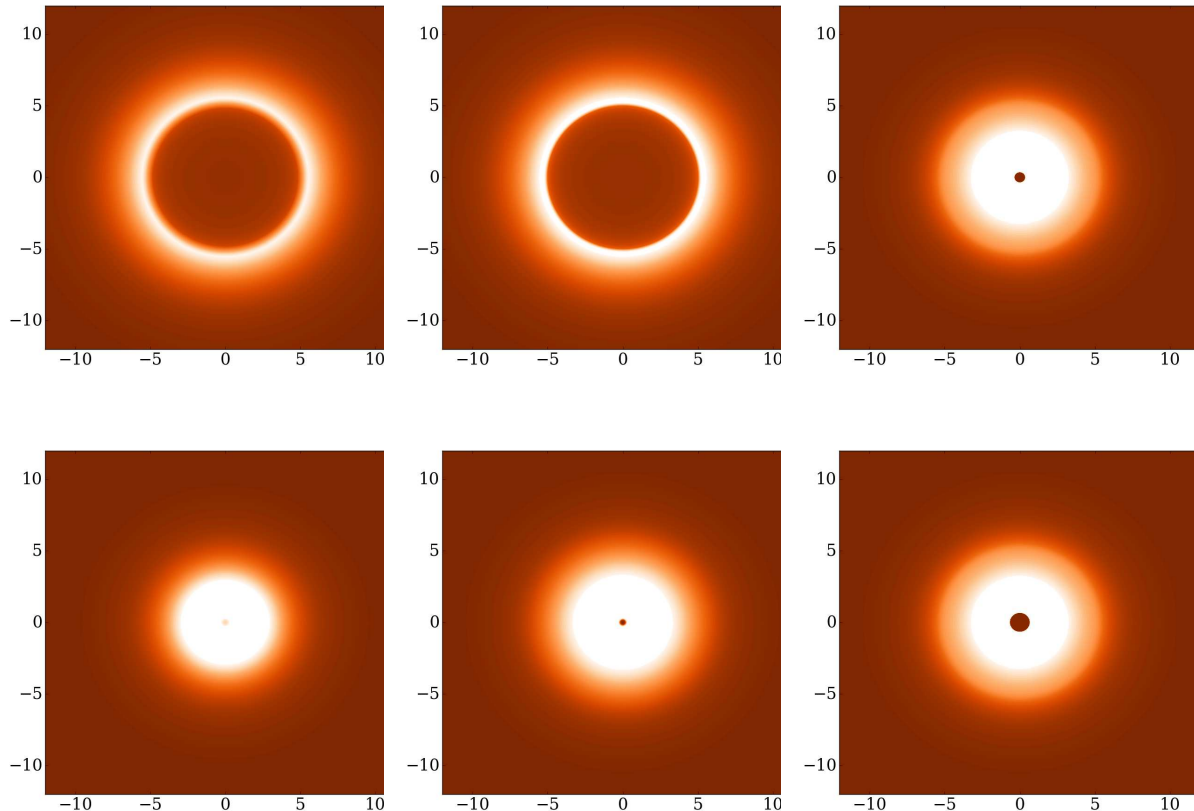


FIG. 8. Shows images in the mm band (200–250 GHz) for the accretion models described in §VI. All the panels use the same (arbitrary) color scale. Top Row: From left to right, the images correspond to the Schwarzschild black hole, JMN-1 naked singularity with  $M_0 = 0.7$ , and JMN-1 with  $M_0 = 0.6$ . The dark spot at the center of the third image is because the inner edge of the grid is at  $r = 10^{-4}M$  rather than at 0. Bottom Row: The left two images correspond to the JMN-2 naked singularity with  $\lambda = 0.8$  and  $\lambda = 0.4$ , respectively. The rightmost panel corresponds to the same model as the one above it (JMN-1,  $M_0 = 0.6$ ), except that the inner edge of the grid in this case is at  $r = 10^{-3}M$ .

in Fig. 8. This is an artifact and is present because we truncate our grid (for numerical reasons) at a finite inner radius  $r_{\min} = 10^{-4}M$  rather than at  $r = 0$ . To illustrate the effect of this truncation, the two panels in the rightmost column of Fig. 8 show images corresponding to the same model (JMN-1  $M_0 = 0.6$ ) except that the upper panel corresponds to  $r_{\min} = 10^{-4}M$ , while the lower panel corresponds to  $r_{\min} = 10^{-3}M$ . The former has a smaller dark spot than the latter, indicating that the spot will disappear in the limit  $r_{\min} \rightarrow 0$ .

Figure 9 shows radial profiles of the image intensity as a function of impact parameter for the five models. The profiles in the mm band (left panel) are quite different from those based on the

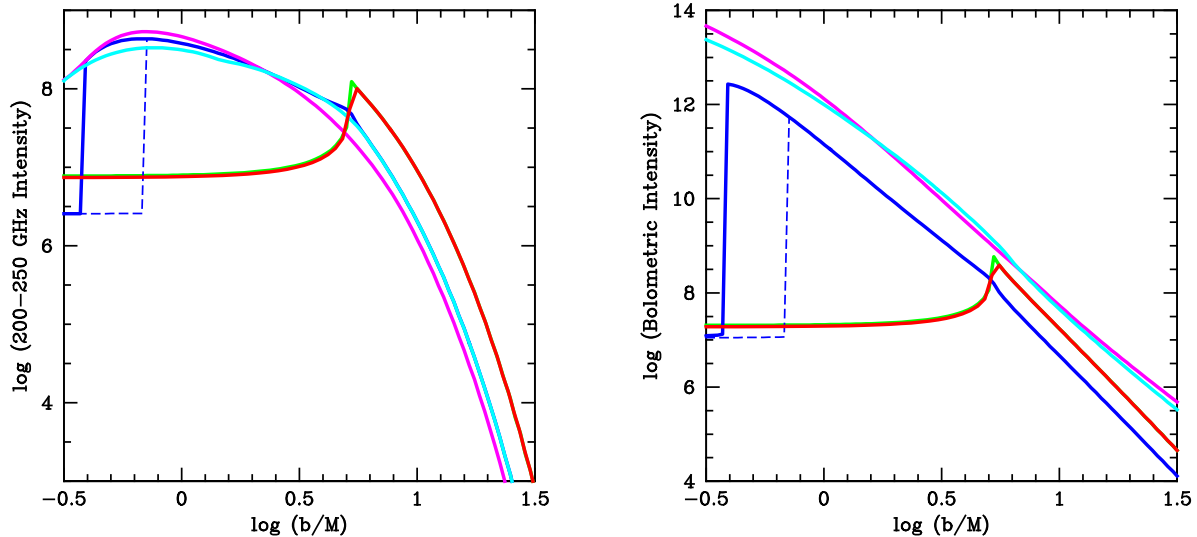


FIG. 9. Left: Radial profiles of the mm band (200–250 GHz) image intensity versus the impact parameter  $b/M$  for the Schwarzschild black hole (red), JMN-1 naked singularity with  $M_0 = 0.7$  (green, under red) and  $M_0 = 0.6$  (blue), and JMN-2 naked singularity with  $\lambda = 0.8$  (magenta) and  $\lambda = 0.4$  (cyan). The solid and dashed blue lines correspond to the same model, but with  $r_{\min} = 10^{-4}M$  (solid) and  $r_{\min} = 10^{-3}M$  (dashed). Right: Corresponding results when the bolometric radiation ( $10^8 - 10^{24}$  Hz) is considered. Note the change in the vertical scale.

bolometric radiation (right panel). The latter are more similar to the profiles shown in Figs. 4 and 5 (but note that those use a linear scale whereas Fig. 9 employs a logarithmic scale).

## VII. CONCLUSION

In this paper, we analyzed images produced by two spherically symmetric models of naked singularities, and compared them with the image produced by a spherically symmetric (Schwarzschild) black hole. We showed that naked singularities could, in some cases, cause shadows that are very similar to those produced by black holes, but in other cases, the two would have very different image structures and would be clearly distinguishable. It follows that a careful investigation of the shadow structure will be needed before the EHT can confirm the existence of an event horizon, and thus a black hole, in Sgr A\*.

To expand on the above point, even if the EHT finds a shadow in Sgr A\*, it will not conclusively

establish the presence of a black hole in this object. The same shadow could be produced by certain naked singularity models. Among the two naked singularity models analyzed in this paper, called JMN-1 and JMN-2, we find that JMN-1 will produce shadows whenever the parameter  $M_0$  (see Eq. 1) lies in the range  $M_0 \geq 2/3$ . This is equivalent to the condition that the matching radius  $R_b$  between the naked singularity interior spacetime and the exterior Schwarzschild spacetime satisfies  $R_b < 3M$ , where  $M$  is the mass of the object. JMN-1 models that do not satisfy the above condition lack a shadow, and produce what we term a “full-moon” image. The JMN-2 model produces a full-moon image for all physically allowed choices of its parameters.

The fact that a shadow does not automatically imply an event horizon was already emphasized by [27], who showed that a model of Sgr A\* with a hard surface will also produce a shadow in mm-band images. The total spectrum would, however, be different. In particular, these authors argued that observations in the infrared would easily distinguish a hard-surface model from a true black hole, because the emission from the surface would dominate in the infrared.

The naked singularity models that produce shadows, viz., JMN-1 with  $M_0 \geq 2/3$ ,  $R_b \leq 3M$ , are different in that their images and spectra at *all wavelengths* are nearly identical to those of a black hole (compare the red and green curves in Figs. 6, 9). Distinguishing these models will thus be much more difficult.

The full-moon images produced by the remaining naked singularity models we considered is also interesting. If such an image were observed, it would certainly rule out a black hole. Whether or not it would confirm the presence of a naked singularity remains to be seen since other non-black hole models might also produce such images.

Similar results to those described in this paper are obtained when we consider the Schwarzschild solution with a scalar field, the so called JNW naked singularity spacetimes [28]. For a range of parameter values, these spacetimes admit a photon sphere, and for other parameter values they do not. In that case as well, the two kinds of models produce shadows and full-moon images, respectively. These results will be reported elsewhere.

Finally, we note that both the JMN-1 and JMN-2 models are characterized by two parameters, namely, the mass parameter  $M_0$  and the matching radius  $R_b$ . As we indicated, the occurrence of naked singularity is stable with respect to variations in these parameters, which is of course still remaining within spherical symmetry. Stability against perturbations of other types, as well as those away from spherical symmetry, is a topic of great interest. Currently we are working from such a perspective, on generalizing these solutions to rotating naked singularity models. It will be physically much more

realistic to compare the shadow structure of such rotating naked singularities with shadows produced by a Kerr black hole.

## ACKNOWLEDGEMENTS

The authors thank the International Centre for Theoretical Sciences, Bangalore, India, for hospitality during some of this work. RN was supported in part by NSF grant AST1312651, and the Black Hole Initiative at Harvard University, which is supported by a grant from the John Templeton Foundation.

- 
- [1] Ghez, A. M., Salim, S., Weinberg, N. N., Lu, J. R. et al., *ApJ*, **689**, 1044 (2008).
  - [2] Schödel, R., Ott, T., Genzel, R., Hofmann, R., et al., *Nature*, **419**, 694 (2002).
  - [3] Kormendy, J., Ho, L. C., *ARAA* **51**, 511 (2013).
  - [4] Broderick, A. E., Loeb, A., Narayan, R., *ApJ* **701**, 1357 (2009).
  - [5] Broderick, A. E., Narayan, R., Kormendy, J., Perlman, E. S., Rieke, M. J., Doeleman, S. S., *ApJ*, **805**, 179 (2015).
  - [6] Narayan, R., McClintock, J. E., *New Astron. Rev.* **51**, 733 (2008).
  - [7] Abramowicz, M. A., Kluzniak, W., Lasota, J.-P., *A&A*, **396**, L31 (2002).
  - [8] Doeleman S. S. et al., *Nature* **455**, 78 (2008).
  - [9] Doeleman S. S. et al., *Science* **338**, 355 (2012).
  - [10] Bardeen, J. M., Press, W. H., Teukolsky, S. A., *ApJ* **178**, 347 (1972).
  - [11] Falcke, H., Melia, F., Agol, E., *Science* **338**, 355 (2000).
  - [12] Luminet, J.-P., *A&A* **75**, 228 (1979).
  - [13] Penrose, R., *Riv. Nuovo Cimento Soc. Ital. Fis.* **1**, 252.
  - [14] Joshi, P. S. , *Gravitational collapse and spacetime singularities*, Cambridge Univ. Press, Cambridge, UK (2007).
  - [15] Joshi, P. S., Malafarina, D., *Int.J.Mod.Phys. D***20**, 2641 (2011).
  - [16] Joshi, P. S., Malafarina, D., Narayan, R., *Class. Quantum Grav.* **28**, 235018 (2011).
  - [17] Joshi, P. S., Malafarina, D., Narayan, R., *Class. Quantum Grav.* **31**, 015002 (2014).
  - [18] Sahu, S., Patil, M., Narasimha, D., Joshi, P. S., *Phys.Rev. D***86**, 063010 (2012).
  - [19] Ohanian, H. C., *American Journal of Physics* **55**, 428 (1987).
  - [20] Bozza, V. *Phys. Rev. D* **66**, 103001 (2002).
  - [21] Bambi, C., *Phys. Rev. D* **87**, 107501 (2013).
  - [22] Jaroszynski, M., Kurpiewski, A., *Astron. Astrophys.* **326**, 419 (1997).
  - [23] Bondi, H., *MNRAS* **112**, 195 (1952).
  - [24] Narayan, R., Zhu, Y., Psaltis, D., Sadowski, A., *MNRAS* **457**, 608 (2016).

- [25] Zhu, Y., Narayan, R., Sadowski, A., Psaltis, D., MNRAS **451**, 1661 (2015).
- [26] Narayan, R., Sadowski, A., Soria, R., MNRAS **469**, 2997 (2017).
- [27] Broderick, A. E., Narayan, R., ApJ **638**, L21 (2006).
- [28] Janis, A. I., Newman, E. T., Winicour, J., Phys. Rev. Lett. **20**, 878 (1968).